Additive manufacturing of Ti-Ni bimetallic structures

Ali Afrouzian, Cory J. Groden, David P. Field, Susmita Bose, and Amit Bandyopadhyay*

W. M. Keck Biomedical Materials Research Laboratory

School of Mechanical and Materials Engineering

Washington State University, Pullman, Washington, 99164, USA.

*Corresponding author email – amitband@wsu.edu

Abstract

Bimetallic structures of nickel (Ni) and commercially pure titanium (CP Ti) were manufactured in three different configurations via directed energy deposition (DED)-based metal additive manufacturing (AM). To understand whether the bulk properties of these three composites are dominated by phase formation at the interface, their directional dependence on mechanical properties was tested. X-ray diffraction (XRD) pattern confirmed the intermetallic NiTi phase at the interface. Microstructural gradient observed at the heat-affected zone (HAZ) areas. The longitudinal samples showed about 12% elongation, while the same was 36% for the transverse samples. During compressive deformation, strain hardening from dislocation accumulation was observed in the CP Ti and transverse samples, but longitudinal samples demonstrated failures similar to a brittle fracture at the interface. Transverse samples also showed shear band formation indicative of ductile failures. Our results demonstrate that AM can design innovative bimetallic structures with unique and directional mechanical properties.

Keywords: Titanium; Nickel; bimetallic structures; additive manufacturing; Directed energy deposition.

1. Introduction

Natural structures often show unique structural features with optimized mechanical properties [1-3]. Design and manufacturing such natural materials having competing performance goals such as strong-yet-stiff require new manufacturing paradigms. However, biomimicry or the emulation of models and architecture to solve complex human problems in a synthetic material is challenging. For instance, the unique crack-arresting and damage tolerance ability of a hierarchical, highly porous bone structure originates from gradual load-transferring between the platelets and intrinsic plastic deformation of fibrils that increases failure resistance [4]. The nacre's extreme strength, stiffness, and fracture toughness highlight its architecture and composition [5] (see **Fig.1A)**. All Nature-inspired materials inherit their bulk properties from their constituents. For instance, bulk properties derive from the rule of the mixture in a layered structure with two different materials. One central question absent in the literature and focused in this study is the possibility of manufacturing layer-by-layer metal-metal bimetallic structures with superior bulk properties that do not follow the rule of mixture. In other words, would it be possible to manufacture a bimetallic structure whose bulk properties are influenced and controlled by the interface properties of the structure rather than the bulk properties of the constituent phases? And that is the novelty of our work, which has been demonstrated in Ni-CP Ti system with the help of DED-based metal AM.

Although conventional tools cannot solve the complexities of different natural materials, AM or 3D printing is a bottom-up, layer-by-layer, cost-effective technique for mimicking intricate prototypes on-demand [6, 7]. Depending on the architecture and elements of the targeted substance, different AM approaches have been used to emulate natural materials. Powder bed fusion (PBF), binder jetting (BJ), and directed energy deposition (DED) are typical examples of AM techniques to print multi-materials [8, 9]; lattice and scaffold structures [10]; and layered and metal/ceramic coatings [11]. Among these, the DED approach can process locally-tuned multi-materials (**Fig.1C**) with different compositions and microstructures efficiently by varying the feedstock powder materials during the printing process [12, 13]. Bimetallic structures are manufactured from two metals and benefit from their electrical, corrosion, and mechanical properties. These multi-compositions would be used in various applications, such as an implant screw shown in **Fig.1B** [14-16]. For instance, Inconel 718 and copper alloy (GRCop-84) structures were fabricated, and the bimetallic composite experienced a 250% and 300% increase than Inconel 718 in thermal diffusivity and conductivity, respectively, due to GRCoP-84 addition [17]. Groden et al. [18] studied the thermal and mechanical properties of Inconel 718 and W-alloy bimetallic structures and found a 100% improvement in thermal diffusivity and compressive yield strength with a 50% reduction in young's modulus to Inconel 718 alone. However, mismatches between the constituents' thermal properties in direct-bonding-based manufacturing can result in crack formation, debonding, and failure [19, 20]. Several techniques to improve part quality include optimized processing parameters such as laser power, scanning speed, and powder feed rate. Besides, the smoothness of the final part can be improved by compositionally graded fabrication which removes the thermal mismatch between different metals [21].

Heat accumulation/cycling during the DED fabrication causes *in situ* high-temperature reactions and phase formation [22-25]. Kang et al. [22] investigated the DED fabrication of pure Ti and Mo powders and found the presence of a graded microstructure along the build direction and phase transformation from hcp-α Ti to bcc-β Ti. Microstructural evolution from equiaxed grains at rapid solidification to a heterogeneous grain structure in post-heating was studied by Wang et al. [25]. It was found that an optimized mechanical property with ~2 times increase in yield strength can be achieved by controlling the thermal history during the DED fabrication. Among different materials available in the powder form, CP Ti is known for its corrosion resistance and biocompatibility, while pure nickel (Ni) with a face-centered-cubic (FCC) crystal structure is known for high electrical and thermal conductivities and good corrosion resistance [26, 27]. Shape memory alloys (SMAs) such as NiTi show an 8% recoverable strain similar to 1% strain recovery in the bone tissue [28, 29]. While NiTi (Nitinol) has been extensively studied, minimal work has been done on the reactive phase formation and microstructural changes in Ni-Ti bilayered structures. Moreover, there is a lack of systematic investigation on the layer-by-layer fabrication of reactive elements such as CP Ti and Ni, corresponding phase formation at the interface, and its influence on mechanical properties. The knowledge gap here is the possibility of fabricating Ni and CP Ti layers and forming various Ni-Ti intermetallic phases at the interface.

This study investigated the processability, microstructure, and mechanical performance of CP Ti and Ni bimetals fabricated via DED-based metal additive manufacturing. It is envisioned that the formation of the reactive phase at the interface would influence the bulk compressive strength and crack arresting capabilities of the final metal composite (MC) part. In addition, it is theorized that the compressive properties are dependent on the interface directions,

which is a reminder of the natural materials. To this end, samples were fabricated in three different configurations: transverse (compressive load is parallel to the build direction or perpendicular to the layers' plane), longitudinal (loading is perpendicular to the build direction), and shear (compressive load is at 45° from the build direction or 45° aligned interface) samples, (see **Fig.1D**). Microstructure, phase analysis, hardness, and quasi-static compression testing were performed on these samples.

2. Materials and methods

2.1. Laser processing of CP Ti to Ni bimetallic structure

The DED system (FormAlloy, Spring Valley, CA) with two powder feeders and a continuous fiber laser to melt deposited powder was utilized to fabricate CP Ti to nickel bimetallic structures. The entire build platform and environment were kept in a controlled argon atmosphere (O_2 < 15 ppm) to limit oxidation. The entire platform and stage can move in X and Y directions, while the laser-head can move in Z direction once one layer is deposited entirely. For this study, spherical CP Ti powder (Grade 2 Ancor-Ti, Hoganas, Sweden) and pure spherical nickel powder (Powder Alloy Corporation, Cincinnati, Ohio) were obtained for printing bimetallic samples. The Cp Ti powder was within a 45-150 μm particle size range, and the Ni powders ranged from 45-75 μm. Transverse and shear samples were printed as 12mm X 12 mm square cross-section patterns, while longitudinal specimens were fabricated as 15mm X 25 mm rectangular cross-section onto a 3.4 mm thick CP Ti substrate, according to the processing parameters outlined in **Table 1**. In this table, energy density (E) is the supplied energy from the laser beam to powder volume and was calculated as [30]:

$$E = \frac{P}{v.h.d}$$

where E (J/mm^3) is the energy density input, P (W) is the laser power, v (mm/s) is scanning speed, h (mm) is hatch spacing, and d (mm) is layer thickness.

2.2. Phase analysis, EBSD, and microstructure

The fabricated samples were sectioned using a low-speed diamond saw to cut in different directions according to the sample types (longitudinal, transverse, and shear). As depicted in **Fig.1D**, a 45° cut was required for shear specimens. After that, samples were mounted in phenolic resin, then sequentially wet-ground using 80-2000 grit SiC sandpaper and polished with 1-0.05 μm alumina-DI water suspension, each for 15 min. For better polishing results, samples were polished for two hours (using VibroMet™ 2 vibratory polisher, Buehler, Lake Bluff, Illinois). In the end, samples were ultrasonically cleaned for 15 min in a 50% ethanol solution.

Samples were scanned using Cu k-alpha radiation at 40kV and 20 mA on a Bruker D8 X-ray Diffractometer equipped with a 2-D General Area Diffraction Detector [GADDS] mounted on a theta-theta goniometer. XRD data were collected on four sequential GADDS frames with an exposure time of 5 min per frame and processed with Bruker DIFFRAC EVA software. For microstructure analysis, samples were cut in cross-section direction, mechanically ground up to 2000 grit SiC sandpaper, and polished up to 0.05 μm alumina-DI water suspension. Kroll's solution (92 mL DI Water, 6 mL HNO3, & 2 mL HF) was utilized to etch the samples by submerging them for 25 s. Field-Emission Scanning Electron Microscopy (FESEM, SEM), electron backscattered diffraction (EBSD) analysis, and Energy Dispersive Spectroscopy (EDS, EDAX by Ametek, PA) were done. For EBSD analysis, samples were also polished via a low

nap cloth and electropolished in 0.05 alumina solution for 1 h at 2 Volts and rinsed in ethanol immediately.

2.3. Hardness and compression test

Vicker's cross-section hardness indents (phase II, Upper Saddle River, NJ) at a 1.96 N load ($HV_{0.2}$) and 15 s dwell time were performed at different areas. A quasi-static compression test [31] (UTM-HYD Instron) was performed at a constant crosshead displacement rate of 0.15 mm/min (~$0.2\times10-4\ s^{-1}$ strain rate in the linear region) until plastic deformation and complete failure. Three samples per configuration were ground to side-length of 5.1 ± 0.05 mm, 5 ± 0.05 mm, and 3.5 ± 0.03 mm from the transverse, longitudinal and, shear samples. The height of these specimens was 10.1 ± 0.05 mm, 11 ± 0.05 mm, and 7.5 ± 0.03 mm, respectively. In general, the average height to side-length ratio was 2. Pure CP Ti and nickel samples were ground to a side length of 4.1 ± 0.05 mm and 8 ± 0.05 mm height.

3. Results

Three different bimetallic configurations were produced via the DED-based reactive-deposition technique, as shown in **Fig.1D**. The manufacturing and characterization flowchart is represented in **Fig.2A**, and the alternate layering of two elements is schematically represented in **Fig.2B**. It is also shown how reactive phases formed at the intermetallic region. The resulting microstructures and mechanical properties, including Vicker's hardness and compression, were investigated to evaluate the effect of adding nickel to a CP Ti for application-specific designs requiring high-toughness capability. In the end, fracture surfaces of compression samples were imaged to understand the failure mechanisms of the bimetallic structure.

3.1. Microstructural analysis of CP Ti-Ni bimetallic structure

Fig. 3 and 4 display the microstructural differences of intermetallic regions at multiple zones. **Fig. 3 (A-E)** shows the microstructure and elemental mapping of the first intermetallic zone. There is a sharp transition from acicular α-phase Ti (**Fig. 3D, E**) in the CP Ti deposition to the equiaxed bimetallic part. According to the EDS, there is no nickel deposition inside the CP Ti region, while the reaction zone displays the presence of both elements. A unique gradient microstructure at the CP Ti and Ni region can be seen and the interface with no cracking and porosity, **Fig. 3B**. The SEM and EDS images of the second layer of CP Ti are shown in **Fig. 4**. There is a smooth transition from Ni to CP Ti with the dendritic-like nickel phase deposited in the CP Ti region (**Fig. 4D**). Also, different size microhardness indents (**Fig. 4B**) are displayed, showing the difference in hardness profile. A larger indent exemplifies the lower hardness value and vice versa. More importantly, no crack initiation at the crack tips was observed even with the presence of spherical residual voids randomly distributed through the interface, **Fig. 4C**. The grain map, grain size range, and inverse pole figure map (IPF) are shown in **Fig. 5**. Different colors in the IPF key show corresponding pole orientations aligned with the specimen surface normal orientation of the CP Ti grains. CP Ti has an hcp crystal structure, and the IPF map shows orientations of the grains forming the Widmanstätten structure typical of transformation microstructures. The <0001> pole figure shows six distinct orientations relating to six <011> planes in a single prior β grain from which this structure evolved. The grains in the transformation structure have an average size of 6.3 μm.

3.2. Phase analysis and hardness

Fig. 6A shows the XRD results at the intermetallic region, demonstrating the existence of HCP α-Ti, FCC nickel, NiTi (B2), and NiTi (B19') phases. B2 is the high-temperature austenite cubic created on heating, and B19' is the low-temperature monoclinic martensite generated on the cooling process [32]. In other words, the transformation sequence for DED laser-processed samples was B19' → B2 on heating and B2 → B19' on cooling. A higher amount of low-temperature martensite phase with a visible yet minor amount of high-temperature austenite phases corresponds to annealing during the laser processing and stabilization of B19' phases. Lower cooling rate due to layer-by-layer manufacturing attributes the annealing, mitigates the larger melt pool and a stronger peak of B19' phase [33]. Also, a long orthogonally oriented α-Ti in the CP Ti nucleates before the β-Ti phases. As a result of heat accumulation during processing, the amount of α-Ti has been decreased [34].

Fig. 6B displays the Vicker's microhardness along the cross-section of the build direction, showing an indication of the transition of hardness from the built plate until the bimetallic parts. The hardness value in all CP Ti regions remained constant, around 250 $HV_{0.2}$, while there was a slight increase in the hardness from 250±6 $HV_{0.2}$ in the substrate to 278±24 $HV_{0.2}$ in printed CP Ti. Hardness values increased to 1043±21 $HV_{0.2}$ and 972±91 $HV_{0.2}$ at the reaction zones, showing around 270% and 50% increase compared to the first CP Ti and fusion zone.

3.3. Compression test

The compression test results for the different configurations and loading directions are presented and compared in **Fig. 7** and **Table 2**. Transverse samples experienced the highest

failure strain and toughness with 36% ± 3% elongations at failure and 163 ± 5 MPa. There are two different slops in the stress-strain curve of the transverse sample, including elastic and plastic strain. The softening and hardening mechanisms represented in the figure are mainly due to the defects such as porosities and grain refinement and dislocation locking during the compression test [35]. On the other side, longitudinal samples reported the highest yield stress with 1187 ± 66 MPa and the lowest failure strain with 0.12 ± 0.005. Also, longitudinal cracks were initiated along with the interfaces and propagated, causing delamination between the layers. After the yielding point in the longitudinal samples, each corresponds to the crack generation at the interfaces and separation between layers. Shear samples display 498 ± 20 MPa, 710 ± 24 MPa, 79 ± 4 MPa, 17% ± 3% for their yield stress, strength, toughness, and failure strain, respectively. As an FCC metal with 12 active slip systems, nickel reported the lowest toughness, yield stress, and compressive strength. In general, bimetallic joints exhibit distinct elastic and plastic deformation zones during the test compared to nickel. Video of the compression tests related to the three different configurations can be found in Appendix A of the supplementary material.

3.4. Fractography

Fig. 8 shows the fracture surface and lines of three different configurations. Faceted fracture surfaces in the delaminated area of the longitudinal samples are reported. Cleavage, known as low strain, low toughness fracture, is the dominant fracture surface of the longitudinal samples and represents the brittle fracture (see **Fig. 8 A, B**). Also, there is no dimple-like fracture presented in the delaminated surface, corresponding to the brittleness of the surfaces [36]. **Fig. 8 C, D** displays the fracture lines of the shear samples. It is evident that sliding of the bottom and

top regions occurred, causing through-interface crack initiation. Longitudinal cracks are also created and stopped at the intermetallic region. There are shear cracks presented in the transverse samples, initiating from the top layer (below the moving jaw or loading point), crossing the interface with the same angle without any crack-branching, and ending at the other sample edge (**Fig. 8 E-G**). Other than that, transverse crack is also created at the lower interface region without causing catastrophic failure. The results indicate the samples' directional dependence of compressive strength, yield strain, and stress. Also, the shear samples display a crack arresting capability at the interface, inhibiting cracks crossing the entire sample causing complete failure.

4. Discussion

Reactive phase formation of the bimetallic structures via DED-based additive manufacturing was investigated in this study to emulate natural materials such as bone and nacre. One of the main objectives of this research was to explore the possibility of manufacturing bimetallic structures of CP Ti and Ni using additive manufacturing. Bonding two dissimilar metals and creating a layer-by-layer structure makes the composite structure's mechanical properties sensitive to part orientation. Another important goal was to study the effect of phase formation on the microstructure and mechanical properties. Multiple powder feeders in the DED system offer flexibility to fabricate composite structures by feeding different materials, yet it needs optimization of processing parameters. Porosity and microcracks were the primary defects in the DED-printed samples. The pores can be initiated from entrapped protective gas in the powder or lack-of-fusion with unmelted powder particles inside [37]. The microcracks and pores are presented in **Fig. 9 (A-C)**, while a delaminated interface is shown in **Fig. 9D.** Delamination and debonding between layers are mainly because of poor bonding resulting from weak shock

resistance during the solidification process and a lack of fusion pores [16] (**Figs**. **9 (A-C)**). Optimization studies were performed to reduce crack formation or delamination in the structure (see **Fig. 9**). **Table 1** highlights the optimized processing parameters necessary to fabricate CP Ti-Ni bimetallic parts. The higher scan speed for nickel composition was chosen to decrease the laser power source at the top of the sample and avoid creating a melt pool. All samples have a hatch spacing of 0.6 mm, and a different layer height of 0.2 mm and 0.05 mm for CP Ti and nickel for transverse and shear samples. Layer heights were 0.25 mm (CP Ti) and 0.05 mm (Ni) for longitudinal samples. Also, the as-printed sample dimensions for shear and the transverse samples were 12mm X 12mm X 15 mm, while it was 15mm X 25mm X 12 mm for the longitudinal samples (**Fig. 1D** and **Fig. 2B**).

The SEM and EDS images (**Figs. 3** and **4**) revealed a compositionally graded microstructure from CP Ti deposition to nickel region. The SEM images of the first CP Ti deposition show a long orthogonally oriented martensite α-Ti laths (or Widmanstatten martensitic titanium microstructure) having an acicular morphology (**Fig. 3 D, E**). This layer of CP Ti has been formed due to the non-equilibrium solidification [38]. Equiaxed NiTi grains have been formed at the intermetallic region. In any areas away from the substrate, conduction is the primary source of heat transfer, while both convection and conduction are presented in the near-substrate area. Thus, going to the second layer of CP Ti deposition, the distance from the substrate increased, resulting in a lower cooling rate along the deposition direction [34]. Consequently, grain morphology changed. As a result of the low solidification rate, large columnar grains were formed in the area away from the substrate along the build direction, **Fig. 4D**. Even with randomly dispersed pores over the interface, there is no crack initiation at the indenter tip, which supports the high-strength and good dimensional stability behavior of NiTi

alloy manufactured during the DED process [39]. One of the most significant factors affecting microstructures and grain size of DED parts is the high solidification rate. As a result, fine acicular titanium grains have been fabricated in the transformation structure instead of equiaxed grains that would be seen upon prolonged cooling (**Fig. 5**). Consequently, a finer grain size would result in higher yield stress according to the Hall-Petch equation [40], given by:

$$\sigma_y = \sigma_0 + kd^{-1/2}$$

where, σ_0 is the friction stress or overall resistance of the lattice to dislocation movement, k is the locking parameter that measures relative hardening, d is the average diameter of grains, and σ_y is the yield stress [41].

NiTi or Nitinol, in commercial terms, is known for shape memory effect, corrosion resistance, biocompatibility, and superelasticity, making it favorable in various applications such as dental, biological, and aerospace [42]. The XRD pattern in **Fig. 6A** shows NiTi austenite and martensite phases. α-Ti grains composed of a long acicular morphology were formed at the layers close to the substrate. Increasing the laser power, going away from the substrate, and decreasing the scan speed reduced the solidification rates and decreased the high-temperature B2 (austenite) phase at the intermetallic region. To understand the high-temperature reaction between CP Ti and Ni during the AM process, Gibbs Free Energy gives an insight even though it considers thermodynamic equilibrium and does not include time for diffusion. Based on that, the higher amount of free energy reduction will show the higher possibilities of the corresponding reaction to occur [24]. The most common reactions between the CP Ti and Ni have been given in the literature as [33]:

$$Ti + Ni \rightarrow NiTi \qquad (i)$$

$$2Ti + Ni \rightarrow NiTi_2 \quad (ii)$$

$$Ti + 3Ni \rightarrow Ni_3Ti \quad (iii)$$

Between 100˚C to 500˚C, ΔG ranges from -584 J/mol to -548 J/mol for equations (i) and (iii), while it ranges from -512 J/mol to -488 J/mol for equation (ii) [43]. Based on Gibbs Free Energy change, it is evident that the formation of Ni_3Ti and NiTi phases is likely that the presence of NiTi component corroborates the phases' XRD findings. However, further studies are necessary to confirm various intermetallic phase formations and their amount.

This effect is further supported by the widened α-Ti grains and its transition to columnar dendritic Ti grains, evidenced by SEM images in **Figs. 3** and **4**. The cross-sectional profile is displayed in **Fig. 6B** and shows the hardness value changes along the build direction. Due to the thin nickel layer, two fusion zones are formed in the first CP Ti-Ni deposition, one in the CP Ti and the other in the Ni regions. Higher hardness values can be attributed to NiTi formation at the interface, supported by the XRD analysis. The hardness profiles have also been backed up by the SEM images, where there is no crack formation and branching at the high-stress concentration area of the indenter tips. Grain refinement and residual stress are the main reasons for the increasing hardness value previously reported [44]. It is evidenced that the hardness value was 548 ± 45 $HV_{0.2}$ at the fusion zone and increased to 1043 ± 21 $HV_{0.2}$ in the first reaction zone. There is a similar pattern in the second depositional layer from the fusion zone to the reaction zone, where the hardness increased from 479 ± 28 $HV_{0.2}$ to 972 ± 91 $HV_{0.2}$.

Compression test results are presented in **Figs. 7, 10,** and **11**. By looking at **Fig. 11 (A, B)**, one can see the formation of shear bands and shear band kink in the CP Ti samples, while nickel shows a flower-like failure. Also, **Fig. 11 (C, D)** represents the after-test micro-level

fracture and shear band formation in the longitudinal sample. It is hypothesized that accumulating those band kinks will lead to crack formation and damage propagation. Shear bands are crystallographic and non-crystallographic band-like deformation, occurring at the highly concentrated plastic flow regions. It is happening due to the inhibition of dislocation slip or twinning. It is well known that CP Ti is an HCP metal with three slip systems, while nickel is an FCC metal with 12 slip systems. Due to the small number of slip systems, dislocation/twinning accumulation (hardening or buildup of deformation stress in the stress-strain curve shown in **Fig. 7**) occurs in a narrow deformation zone. In such cases, shear banding can act as an alternative non-crystallographic deformation mode, often associated with a sudden drop in the local flow stress [45] (see **Fig. 7**). As such, shear banding is a softening mechanism. Having many fractured areas in the nickel contributes to the higher number of slip systems causing easier dislocation flow because of the high Schmid factor as follows:

$$\tau_{rss} = \frac{P}{A} cos\emptyset cos\theta$$

where τ_{rss} is resolved shear stress, P is force, A is cross-section, $\emptyset$ and θ are angles between load direction, slip plane normal, and slip direction, respectively. In the following, $cos\emptyset cos\theta$ is known as the Schmid factor. According to Schmid's law, plastic deformations begin when the shear stress resolved along the slip direction on the slip plane reaches a critical value [45]. On the other hand, composite samples have different compressive and fracture behavior. In the longitudinal samples, stress increases linearly to about 1100 MPa and then drops slightly due to the formation of two longitudinal cracks, presented in **Fig. 10**. Two more drops in stress in the longitudinal sample are attributed to the crack propagation and debonding between intermetallic layers. The stress remained almost constant before complete failure, which corresponds to

detachment of the nickel layer due to brittle failure at the interface (**Fig. 8**). In other words, there is no work hardening after the yield point, showing perfectly plastic behavior. According to **Figs. 7, 8,** and **10**, the main failure modes of the transverse sample are the formation of shear band in the CP Ti region, intermetallic crack formation, and peeling of the interface. Strain or work hardening results from a significant increase in dislocations and their interactions, reducing dislocation mobility. As a result, larger stresses must be applied so that additional deformation may occur [46]. Other than grain size, there are three main strain hardening mechanisms in the crystallographic metals, including Frank-Read source and forest (Baily-Hirsch) hardening. So, the stress equation can be written as follows:

$$\sigma_y = \sigma_0 + kd^{-1/2} + \alpha\mu b\sqrt{\rho_d} + \frac{\mu b}{L}\cos\left(\frac{\varphi_c}{2}\right)$$

where, α is a constant depending on crystal structure, μ is shear modulus, b is burgers vector, L is the distance between two obstacles (Frank-Read source size), φ_c is the critical angle of glide dislocation around the obstacle (which is taken as a material parameter), and ρ_d is dislocation density. In the transverse sample, dislocations can be stuck by the pores created during manufacturing (Frank-Read source). In addition, by looking at **Fig. 8 (E-G)**, one can figure out that crack is initiated at the CP Ti region due to dislocation pile-up at the shear band. Shear bands propagated until they reached the interfaces with more slip systems, resulting in more dislocation annihilation and crack growth until complete failure [47]. Failure mode in the shear sample is different from transverse and longitudinal ones. With creating an aligned interface, failure will happen due to the sliding between the top and bottom parts. Accordingly, the strain was going up with no hardening effect, initial cracks formed, and two regions failed at the

bonding area. One hardening at the end of the stress-strain curve is attributed to the macroscopic friction between the layers.

5. Conclusion

In this work, reactive phase formation via DED-based metal additive manufacturing for producing directionally dependent architecture was investigated to envision the possibility of creating nature-inspired materials. Three different composite configurations consisting of nickel and CP Ti were considered and printed by changing the deposited feedstock. NiTi phase formed at the interface of nickel and Ti, influenced the bulk structure's properties. Vicker's hardness experienced 2.76 times increased in the reaction zone compared to CP Ti region and showed a fluctuating behavior to build direction. SEM and EDS presented a compositionally gradient change in microstructure from the pure metal to interface. As such, acicular titanium in the CP Ti region turned to equiaxed grains at the interfaces. The compression test revealed that shear band formation as a plastic deformation mechanism, toughness, and yield stress depends on the loading direction or sample configuration. While the primary fracture mode in the longitudinal sample was brittle debonding, transverse loading caused shear band formation and strain localization with work hardening in the stress-strain plot. The aligned interface, the shear sample, experienced a sliding between the top and bottom region during the compression and showed lower strength and yield than two other composites.

Acknowledgments

The authors acknowledge financial support from the National Science Foundation under grant # CMMI 1934230 (PI- Bandyopadhyay). The authors also acknowledge financial support from the National Institute of Arthritis and Musculoskeletal and Skin Diseases of the National Institutes of Health under Award Number R01 AR067306 (PI- Bandyopadhyay). The authors are also grateful for financial assistance from JCDREAM (Seattle, WA) for a capital equipment grant to purchase the powder bed-based metal 3D Printer at WSU. The content is solely the authors' responsibility and does not necessarily represent the official views of the National Institutes of Health.

References

[1] H. D. Espinosa, A.L. Juster, F.J. Latourte, O.Y. Loh, D. Gregoire, P.D. Zavattieri, Tablet-level origin of toughening in abalone shells and translation to synthetic composite materials, Nat Commun 2 (2011) 173.

[2] U. G. Wegst, H. Bai, E. Saiz, A.P. Tomsia, R.O. Ritchie, Bioinspired structural materials, Nat Mater 14(1) (2015) 23-36.

[3] U. G. K. Wegst, M.F. Ashby, The mechanical efficiency of natural materials, Philosophical Magazine 84(21) (2004) 2167-2186.

[4] A. Bandyopadhyay, K.D. Traxel, S. Bose, Nature-inspired materials and structures using 3D Printing, Mater Sci Eng R Rep 145 (2021).

[5] F. Greco, L. Leonetti, A. Pranno, S. Rudykh, Mechanical behavior of bio-inspired nacre-like composites: A hybrid multiscale modeling approach, Composite Structures 233 (2020).

[6] A.R. Studart, Additive manufacturing of biologically-inspired materials, Chem Soc Rev 45(2) (2016) 359-76.

[7] Y. Yang, X. Song, X. Li, Z. Chen, C. Zhou, Q. Zhou, Y. Chen, Recent Progress in Biomimetic Additive Manufacturing Technology: From Materials to Functional Structures, Adv Mater (2018) e1706539.

[8] B. Onuike, A. Bandyopadhyay, Functional Bimetallic Joints of Ti6Al4V to SS410, Addit Manuf 31 (2020).

[9] K. D. Traxel, A. Bandyopadhyay, Naturally architected microstructures in structural materials via additive manufacturing, Addit Manuf 34 (2020).

[10] Y. Amani, S. Dancette, P. Delroisse, A. Simar, E. Maire, Compression behavior of lattice structures produced by selective laser melting: X-ray tomography based experimental and finite element approaches, Acta Materialia 159 (2018) 395-407.

[11] Y. Zhang, A. Bandyopadhyay, Influence of Compositionally Graded Interface on Microstructure and Compressive Deformation of 316L Stainless Steel to Al12Si Aluminum Alloy Bimetallic Structures, ACS Appl Mater Interfaces 13(7) (2021) 9174-9185.

[12] A. du Plessis, I. Yadroitsava, I. Yadroitsev, Effects of defects on mechanical properties in metal additive manufacturing: A review focusing on X-ray tomography insights, Materials & Design 187 (2020).

[13] T. Gualtieri, A. Bandyopadhyay, Additive manufacturing of compositionally gradient metal-ceramic structures: Stainless steel to vanadium carbide, Materials & Design 139 (2018) 419-428.

[14] B. E. Carroll, R.A. Otis, J.P. Borgonia, J.-o. Suh, R.P. Dillon, A.A. Shapiro, D.C. Hofmann, Z.-K. Liu, A.M. Beese, Functionally graded material of 304L stainless steel and inconel 625 fabricated by directed energy deposition: Characterization and thermodynamic modeling, Acta Materialia 108 (2016) 46-54.

[15] B. Li, C. Han, C.W.J. Lim, K. Zhou, Interface formation and deformation behaviors of an additively manufactured nickel-aluminum-bronze/15-5 PH multimaterial via laser-powder directed energy deposition, Materials Science and Engineering: A 829 (2022).

[16] K. D. Traxel, A. Bandyopadhyay, Modeling and experimental validation of additively manufactured tantalum-titanium bimetallic interfaces, Materials & Design 207 (2021).

[17] B. Onuike, A. Bandyopadhyay, Additive manufacturing of Inconel 718 – Ti6Al4V bimetallic structures, Additive Manufacturing 22 (2018) 844-851.

[18] C. Groden, K.D. Traxel, A. Afrouzian, E. Nyberg, A. Bandyopadhyay, Inconel 718-W7Ni3Fe bimetallic structures using directed energy deposition-based additive manufacturing, Virtual and Physical Prototyping (2022) 1-11.

[19] C. Rock, P. Tarafder, L. Ives, T. Horn, Characterization of copper & stainless steel interface produced by electron beam powder bed fusion, Materials & Design 212 (2021).

[20] L. Yan, Y. Chen, F. Liou, Additive manufacturing of functionally graded metallic materials using laser metal deposition, Additive Manufacturing 31 (2020).

[21] D. Gu, X. Shi, R. Poprawe, D.L. Bourell, R. Setchi, J. Zhu, Material-structure-performance integrated laser-metal additive manufacturing, Science 372(6545) (2021).

[22] N. Kang, X. Lin, M.E. Mansori, Q.Z. Wang, J.L. Lu, C. Coddet, W.D. Huang, On the effect of the thermal cycle during the directed energy deposition application to the in-situ production of a Ti-Mo alloy functionally graded structure, Additive Manufacturing 31 (2020).

[23] N. Sommer, P. Kluge, F. Stredak, S. Eigler, H. Hill, T. Niendorf, S. Böhm, Additive Manufacturing of Compositionally-Graded AISI 316L to CoCrMo Structures by Directed Energy Deposition, Crystals 11(9) (2021).

[24] K. D. Traxel, A. Bandyopadhyay, Reactive-deposition-based additive manufacturing of Ti-Zr-BN composites, Additive Manufacturing 24 (2018) 353-363.

[25] Z. Wang, X. Lin, N. Kang, J. Chen, Y. Tang, H. Tan, X. Yu, H. Yang, W. Huang, Directed energy deposition additive manufacturing of a Sc/Zr-modified Al–Mg alloy: Effect of thermal history on microstructural evolution and mechanical properties, Materials Science and Engineering: A 802 (2021).

[26] T. Nagase, T. Hori, M. Todai, S.-H. Sun, T. Nakano, Additive manufacturing of dense components in beta-titanium alloys with crystallographic texture from a mixture of pure metallic element powders, Materials & Design 173 (2019).

[27] Z. Zhou, L. Huang, Y. Shang, Y. Li, L. Jiang, Q. Lei, Causes analysis on cracks in nickel-based single crystal superalloy fabricated by laser powder deposition additive manufacturing, Materials & Design 160 (2018) 1238-1249.

[28] H. Deng, Y. Chen, S. Li, C. Chen, T. Zhang, M. Xu, D. Ji, Microstructure, mechanical properties and transformation behavior of friction stir welded Ni50.7Ti49.3 alloy, Materials & Design 189 (2020).

[29] M. Elahinia, N. Shayesteh Moghaddam, M. Taheri Andani, A. Amerinatanzi, B.A. Bimber, R.F. Hamilton, Fabrication of NiTi through additive manufacturing: A review, Progress in Materials Science 83 (2016) 630-663.

[30] K. D. Traxel, D. Malihi, K. Starkey, A. Bandyopadhyay, Model-driven directed-energy-deposition process workflow incorporating powder flowrate as key parameter, Manufacturing Letters 25 (2020) 88-92.

[31] E. ASTM, Standard test methods of compression testing of metallic materials at room temperature, West Conshohocken, PA: ASTM International (2000) 98-105.

[32] P. R. Halani, I. Kaya, Y.C. Shin, H.E. Karaca, Phase transformation characteristics and mechanical characterization of nitinol synthesized by laser direct deposition, Materials Science and Engineering: A 559 (2013) 836-843.

[33] C. Wang, X.P. Tan, Z. Du, S. Chandra, Z. Sun, C.W.J. Lim, S.B. Tor, C.S. Lim, C.H. Wong, Additive manufacturing of NiTi shape memory alloys using pre-mixed powders, Journal of Materials Processing Technology 271 (2019) 152-161.

[34] X. Lin, T.M. Yue, H.O. Yang, W.D. Huang, Microstructure and phase evolution in laser rapid forming of a functionally graded Ti–Rene88DT alloy, Acta Materialia 54(7) (2006) 1901-1915.

[35] M. Hamid, M.S. Saleh, A. Afrouzian, R. Panat, H.M. Zbib, Modeling of porosity and grain size effects on mechanical behavior of additively manufactured structures, Additive Manufacturing 38 (2021).

[36] A. Moridi, A.G. Demir, L. Caprio, A.J. Hart, B. Previtali, B.M. Colosimo, Deformation and failure mechanisms of Ti–6Al–4V as built by selective laser melting, Materials Science and Engineering: A 768 (2019).

[37] B. Li, H. Zheng, C. Han, K. Zhou, Nanotwins-containing microstructure and superior mechanical strength of a Cu–9Al–5Fe–5Ni alloy additively manufactured by laser metal deposition, Additive Manufacturing 39 (2021).

[38] H. Attar, M. Bönisch, M. Calin, L.-C. Zhang, S. Scudino, J. Eckert, Selective laser melting of in situ titanium–titanium boride composites: Processing, microstructure and mechanical properties, Acta Materialia 76 (2014) 13-22.

[39] H. E. Karaca, S.M. Saghaian, G. Ded, H. Tobe, B. Basaran, H.J. Maier, R.D. Noebe, Y.I. Chumlyakov, Effects of nanoprecipitation on the shape memory and material properties of an Ni-rich NiTiHf high temperature shape memory alloy, Acta Materialia 61(19) (2013) 7422-7431.

[40] C. E. Carlton, P.J. Ferreira, What is behind the inverse Hall–Petch effect in nanocrystalline materials?, Acta Materialia 55(11) (2007) 3749-3756.

[41] N. Abdolrahim, H.M. Zbib, D.F. Bahr, Multiscale modeling and simulation of deformation in nanoscale metallic multilayer systems, International Journal of Plasticity 52 (2014) 33-50.

[42] J.J. Marattukalam, A.K. Singh, S. Datta, M. Das, V.K. Balla, S. Bontha, S.K. Kalpathy, Microstructure and corrosion behavior of laser processed NiTi alloy, Mater Sci Eng C Mater Biol Appl 57 (2015) 309-13.

[43] V. S. Klimin, A.A. Rezvan, O.A. Ageev, V.F. Lukichev, K.V. Rudenko, Effect of the sublayer material on the formation of electrical contact and the growth rate of carbon nanotubes

in a low-temperature plasma using the example of Ni/Ti/Si and Fe/W/Si structures, International Conference on Micro- and Nano-Electronics 2018, 2019.

[44] I. Shishkovsky, I. Yadroitsev, I. Smurov, Direct Selective Laser Melting of Nitinol Powder, Physics Procedia 39 (2012) 447-454.

[45] N. Jia, F. Roters, P. Eisenlohr, C. Kords, D. Raabe, Non-crystallographic shear banding in crystal plasticity FEM simulations: Example of texture evolution in α-brass, Acta Materialia 60(3) (2012) 1099-1115.

[46] H. Askari, H. M. Zbib, X. Sun, Multiscale Modeling of Inclusions and Precipitation Hardening in Metal Matrix Composites: Application to Advanced High-Strength Steels, Journal of Nanomechanics and Micromechanics 3(2) (2013) 24-33.

[47] T. Sedlatschek, J. Lian, W. Li, M. Jiang, T. Wierzbicki, M.Z. Bazant, J. Zhu, Large-deformation plasticity and fracture behavior of pure lithium under various stress states, Acta Materialia 208 (2021).

Appendix A. Supplementary data

Supplementary documents related to compression tests and videos can be found in the online version.

Table and Figure captions

Table. 1. Processing parameters of DED-fabricated CP Ti-Ni bimetallic structures.
Table 2. Quasi-static compression test results.

Fig. 1. Examples of layered structures presented in nature and industry that can be inspired for the next generation bimetallic multi-functional composite structure. (A) schematics of nacre's hierarchical design [48], (B) schematics of titanium tantalum implant screw, (C) schematics of DED fabrication process of CP Ti-nickel bimetallic layered structure, (D) different samples' configuration.

Fig. 2. Illustrative DED processing and fabricated bimetallic structure (A) manufacturing and characterization diagram, (B) alternate material deposition process and intermetallic phase microstructure.

Fig. 3. Microstructure and EDS at the sample's cross-section from the first CP Ti-Ni deposition layers. (A), (B) lower magnification interface and its elemental mapping. (C) higher magnification of the interface. (D) First layer of CP Ti in lower magnification. (E) needle-like structure of first layer of CP Ti.

Fig. 4. Microstructure and EDS at the sample's cross-section from the second CP Ti-Ni deposition layers. (A) second layer of CP Ti deposited on the top of the nickel. (B) lower magnification of nickel region. (C) higher magnification of nickel region showing micro-voids and hardness indent, no cracking was observed around the indent tip. (D) Microstructure and elemental mapping of second layer of CP Ti.

Fig. 5. Microstructure and EBSD pattern showing inverse pole figure (IPF) maps and average effective grain size distribution of CP Ti.

Fig. 6. (A) Phase analysis, (B) Vicker's microhardness profile for the CP Ti-Ni bimetallic structures.

Fig. 7. Quasi-static compression test results for different samples' configuration.

Fig. 8. Surface and cross-sectional images from the damaged area. (A, B) longitudinal, (C, D) shear, (E, F, G) transverse samples.

Fig. 9. Cracks and pores generated during the printing without processing parameters' optimization. (A-C) Crack propagation at the interface, (D) delamination and macro-cracks of the built sample.

Fig. 10. Surface and cross-sectional images from the damaged area. (A, B) longitudinal, (C, D) shear, (E, F, G) transverse samples.

Fig. 11. (A, B) Failure of pure CP Ti and nickel, (C, D) microscopic cracks and micron level shear band formation in the after-test longitudinal sample

Transverse and shear samples

Final dimension (mm^3)	section	Layer no.	Laser power (W)	Hatch speed (mm/s)	Hatch spacing (mm)	Layer height (µm)	Energy density (J/mm^3)
12×12×15	CP Ti	1-20	300	12.5	0.6	0.2	200
		21-40	250	20.83		0.05	400
	CP Ti	41-60	300	12.5		0.2	200
	nickel	61-80	250	20.83		0.05	400
	CP Ti	81-90	300	12.5		0.2	200

Longitudinal samples

Final dimension (mm^3)	section	Layer no.	Laser power (W)	Hatch speed (mm/s)	Hatch spacing (mm)	Layer height (µm)	Energy density (J/mm^3)
15×25×12	CP Ti	1-20	300	12.5	0.6	0.25	160
	nickel	21-30	280	20.83		0.05	448
	CP Ti	31-50	300	12.5		0.25	160
	nickel	51-60	280	20.83		0.05	448
	CP Ti	61-70	300	12.5		0.25	160

Table. 1. Processing parameters of DED-fabricated CP Ti-Ni bimetallic structures.

Table 2. Quasi-static compression test results.

Sample	*Yield Stress (MPa)*	*Compressive Strength (MPa)*	*Toughness (N.m^-2) * 10^6*	*Failure strain*
shear	498 ± 20	710 ± 24	79 ± 4	0.17 ± 0.03
Transvers	625 ± 4	1004 ± 43	163 ± 5	0.36 ± 0.03
Longitudinal	795 ± 44	1187 ± 66	94 ± 7	0.12 ± 0.005
nickel	66 ± 5	83 ± 10	11 ± 0.9	0.17 ± 0.008
CP Ti	519 ± 12	817 ± 15	146 ± 16	0.25 ± 0.012

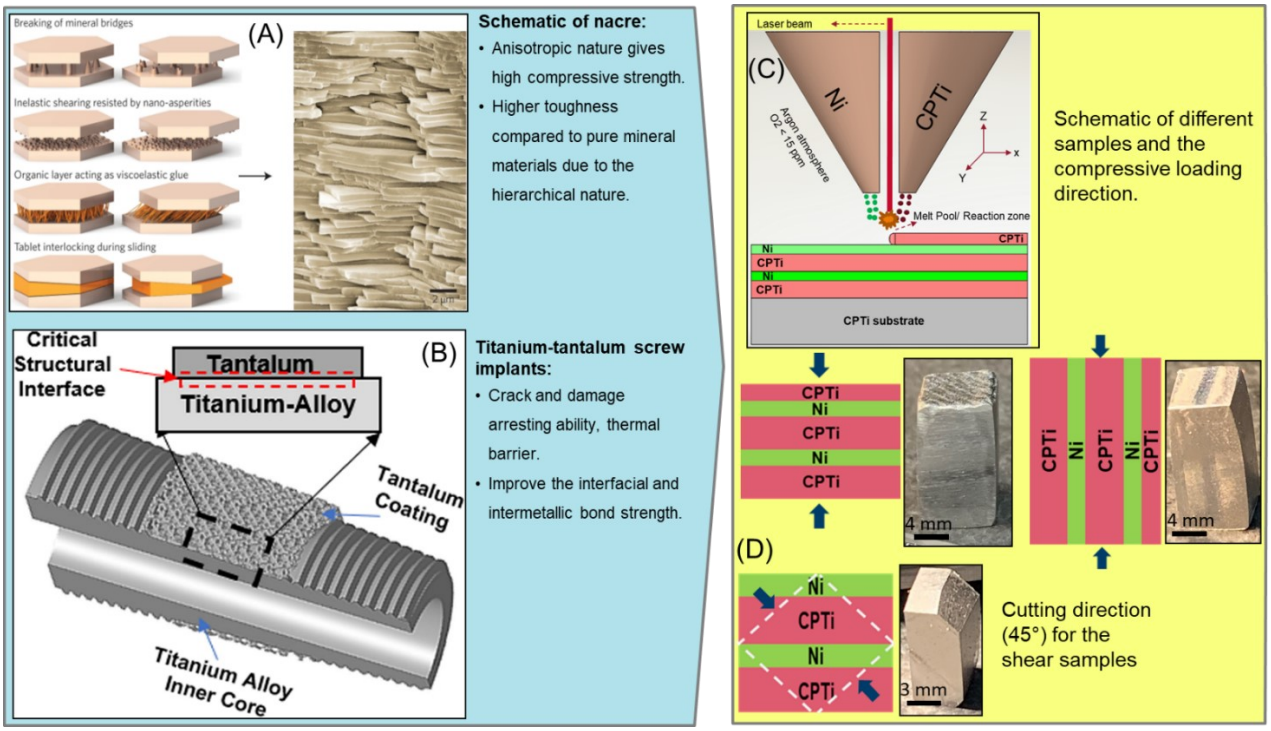

Fig. 1. Examples of layered structures presented in nature and industry can be inspired for the next generation bimetallic multi-functional composite structure. (A) schematics of nacre's hierarchical design [2], (B) schematics of titanium tantalum implant screw [16], (C) schematics of DED fabrication process of CP Ti-nickel bimetallic layered structure, (D) different configurations of the samples.

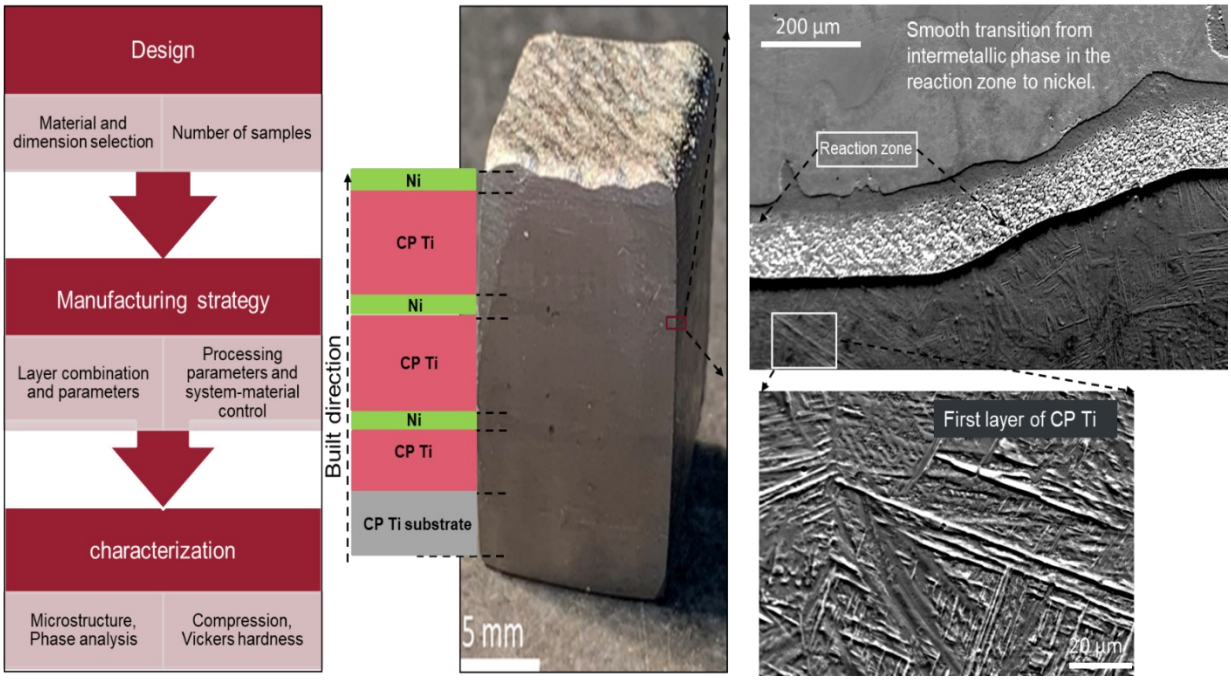

Fig. 2. Illustrative DED processing and fabricated bimetallic structure (A) manufacturing and characterization diagram, (B) alternate material deposition process, and intermetallic phase microstructure.

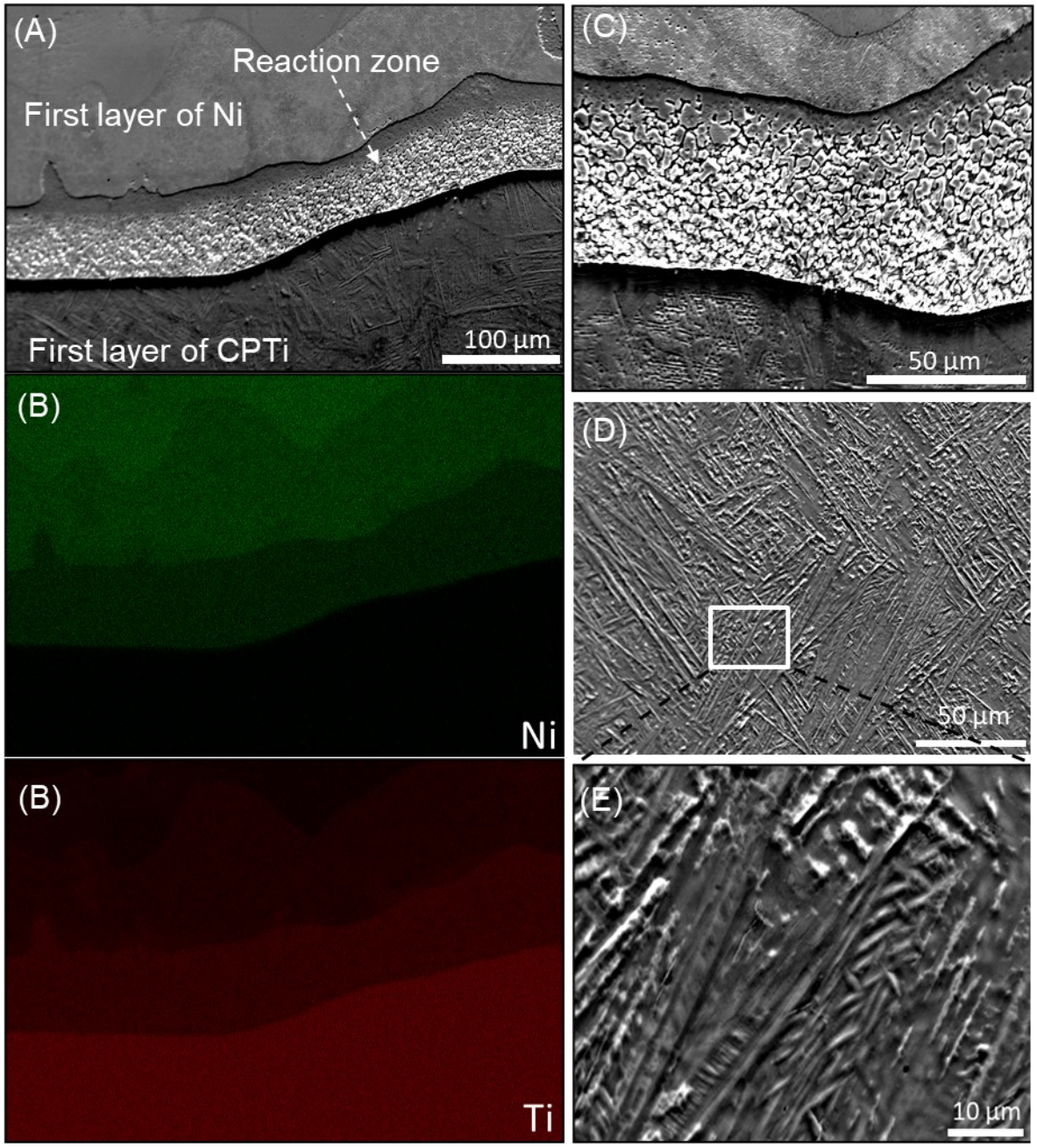

Fig. 3. Microstructure and EDS at the sample's cross-section from the first CP Ti-Ni deposition layers. (A), (B) lower magnification interface and its elemental mapping. (C) higher magnification of the interface. (D) The first layer of CP Ti is in lower magnification. (E) needle-like structure of the first layer of CP Ti.

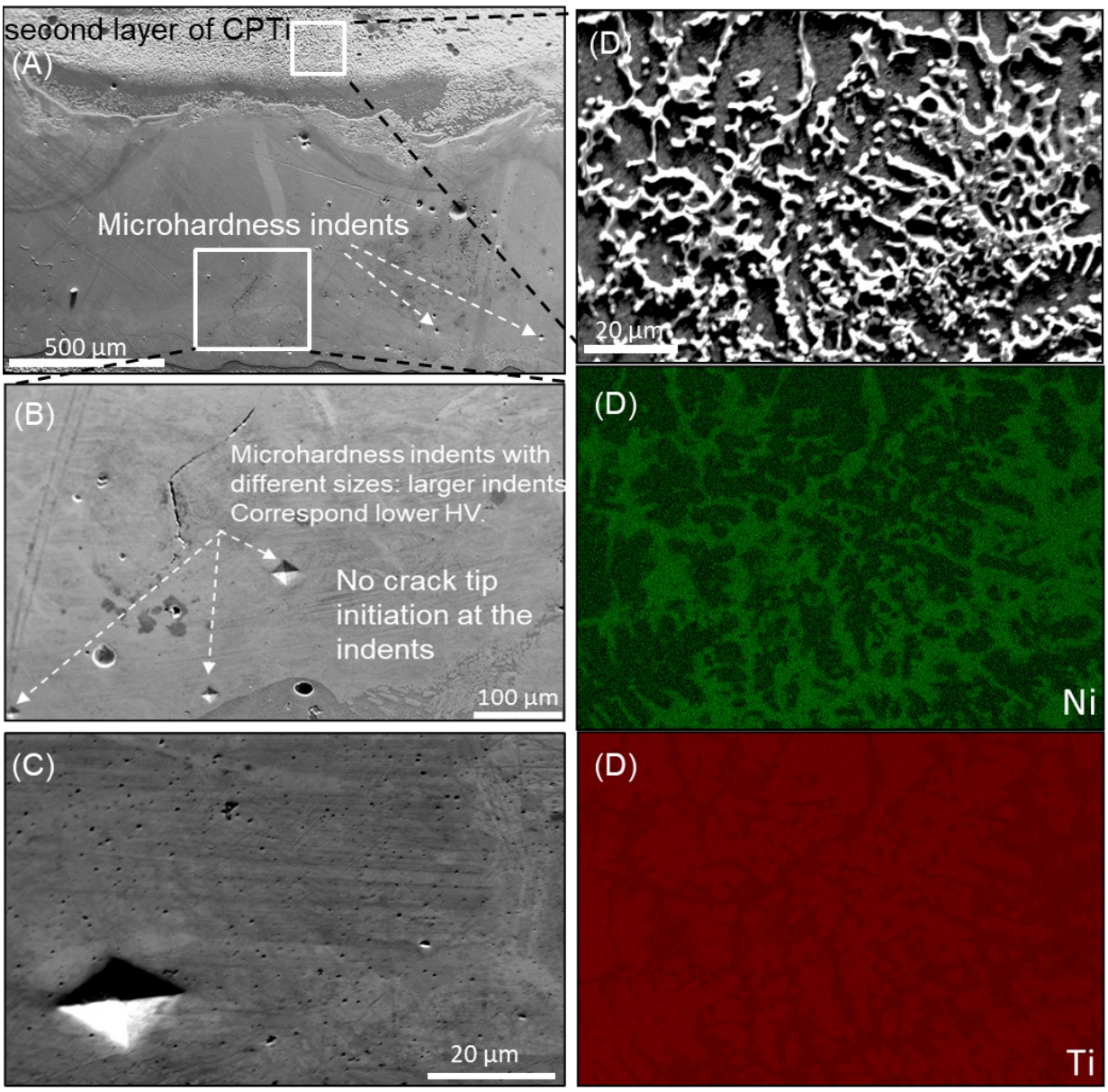

Fig. 4. Microstructure and EDS at the sample's cross-section from the second CP Ti-Ni deposition layers. (A) the second layer of CP Ti is deposited on top of the nickel. (B) lower magnification of nickel region. (C) higher magnification of nickel region showing micro-voids and hardness indent, no cracking was observed around the indenting tip. (D) Microstructure and elemental mapping of the second layer of CP Ti.

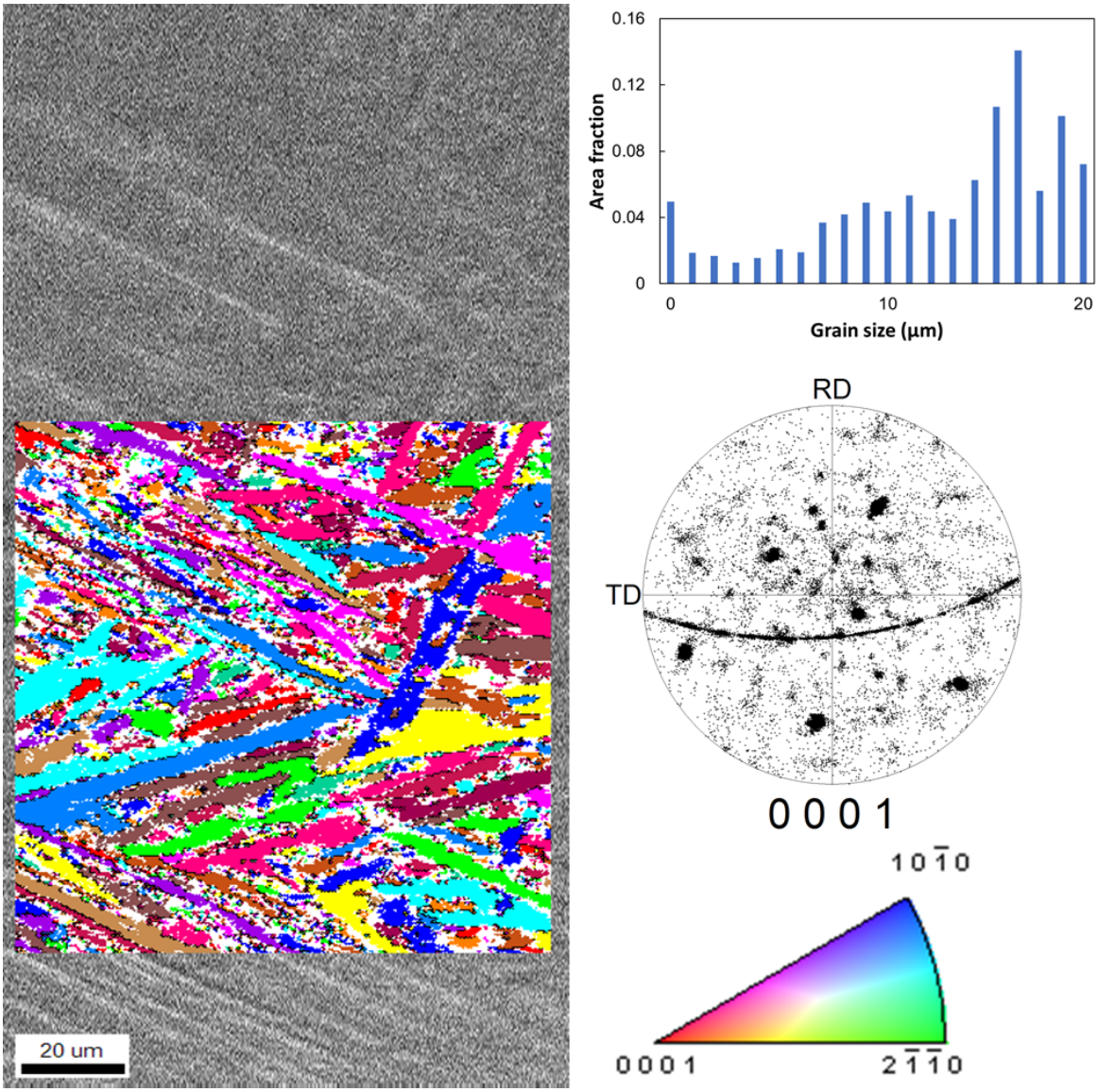

Fig. 5. Microstructure and EBSD pattern show inverse pole figure (IPF) maps and average effective CP Ti grain size distribution.

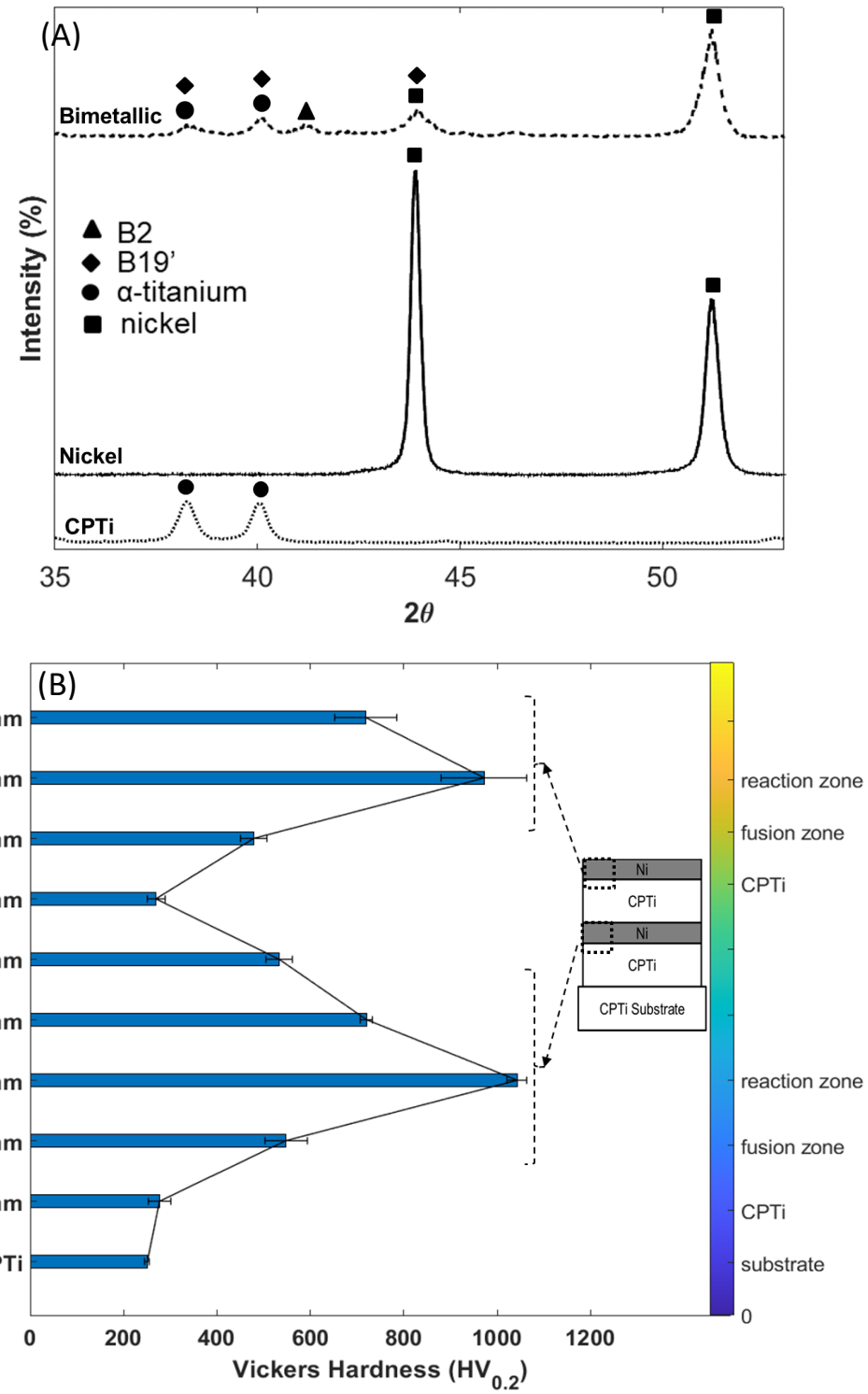

Fig. 6. (A) Phase analysis, (B) Vicker's microhardness profile for the CP Ti-Ni bimetallic structures.

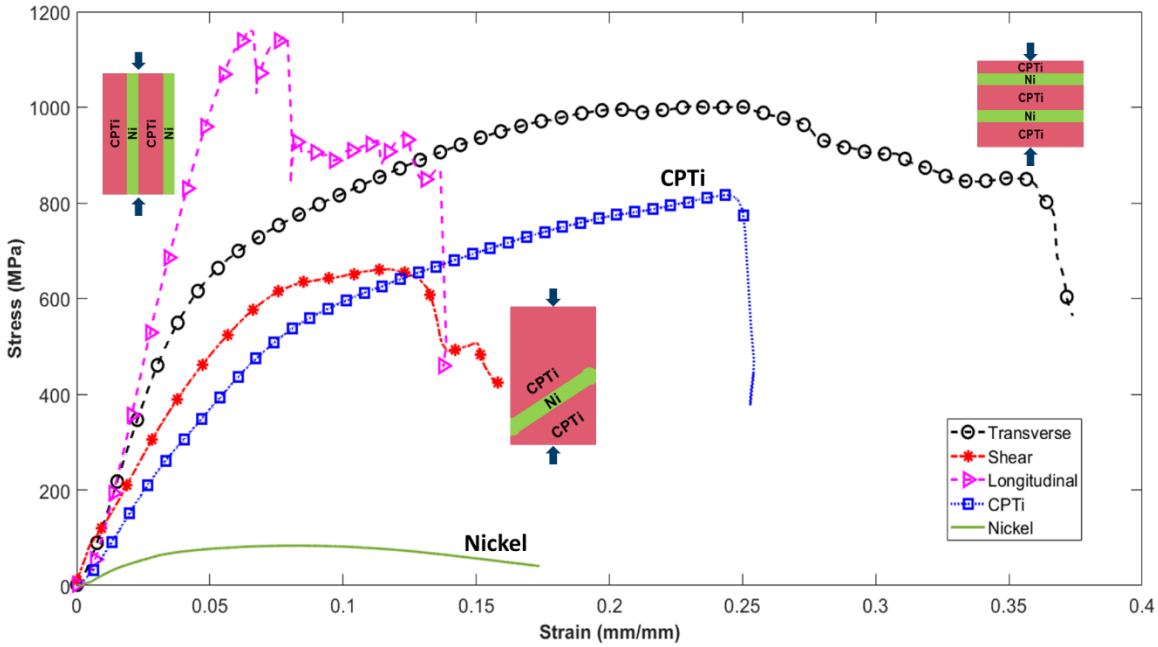

Fig. 7. Quasi-static compression test results for different samples' configurations.

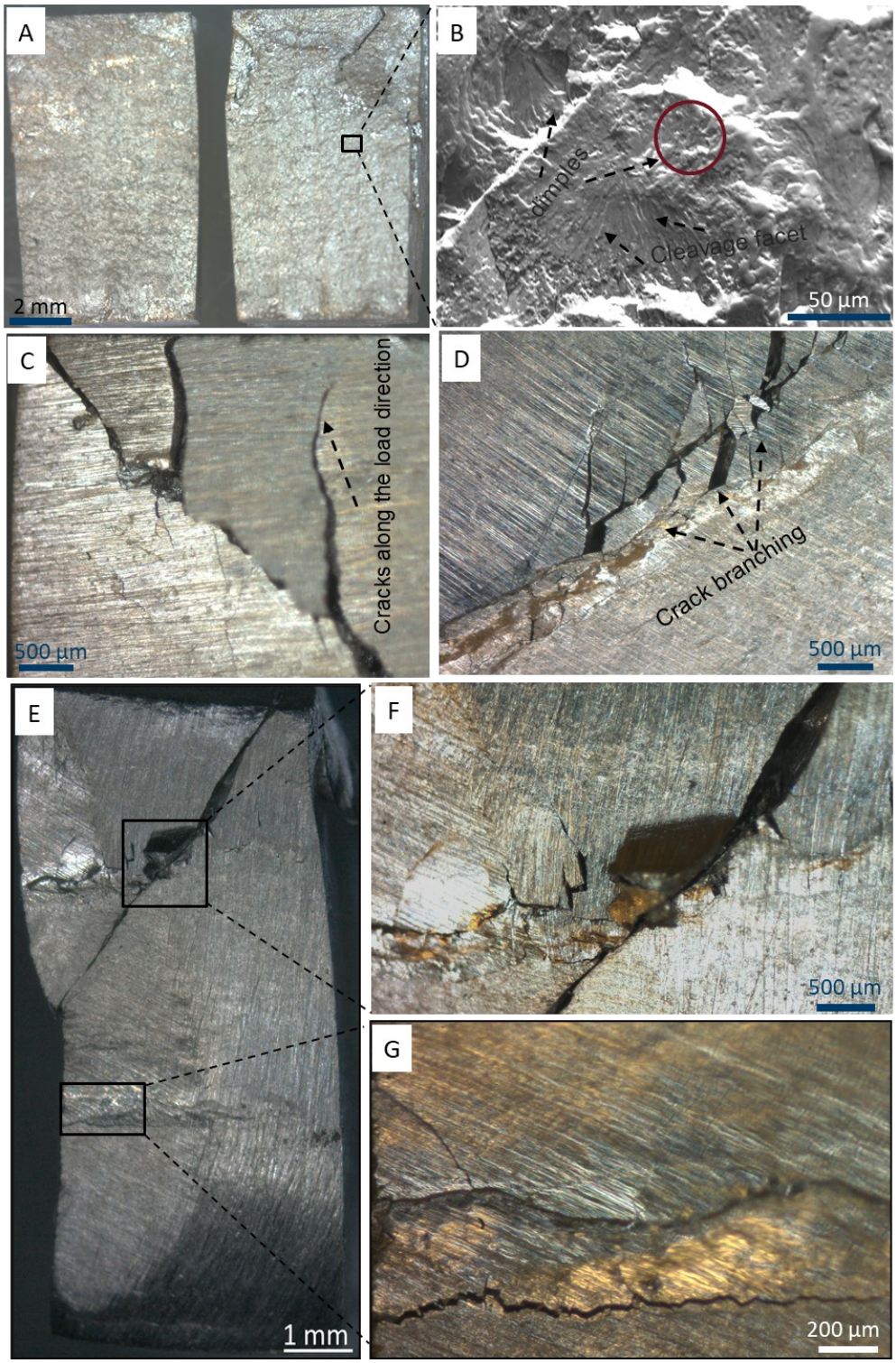

Fig. 8. Surface and cross-sectional images from the damaged area. (A, B) longitudinal, (C, D) shear, (E, F, G) transverse samples.

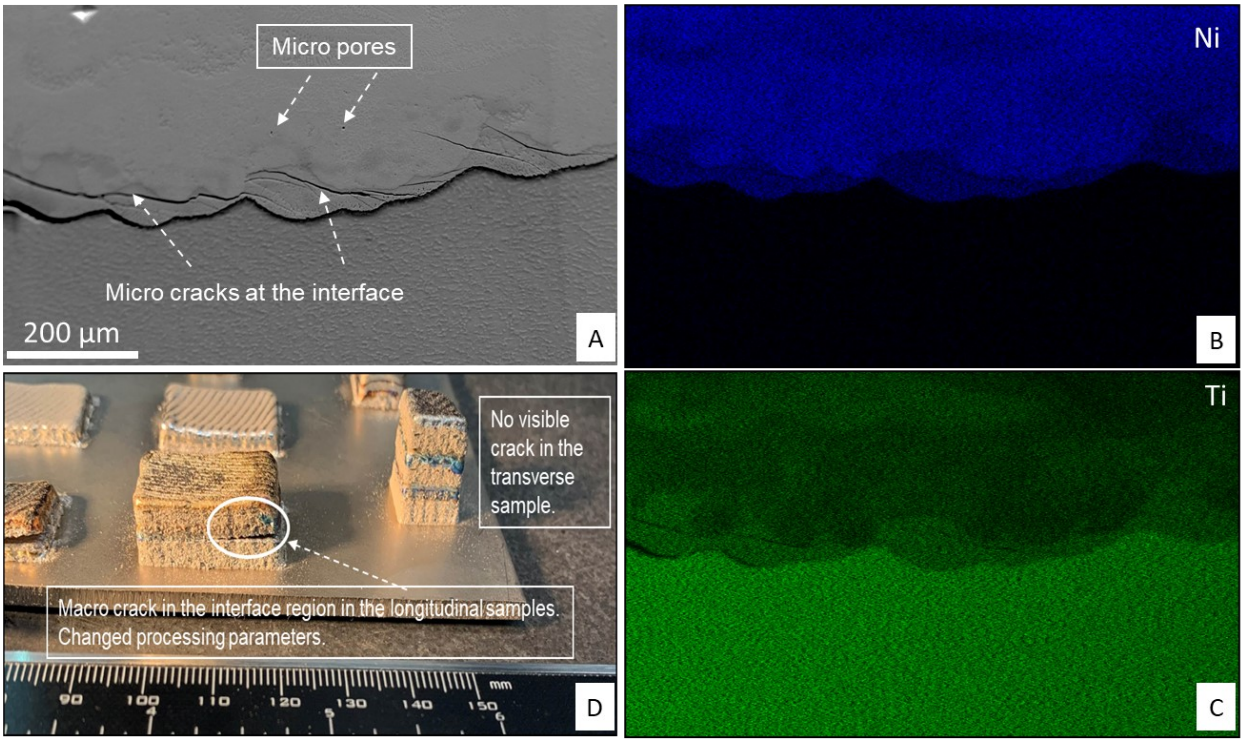

Fig. 9. Cracks and pores generated during the printing without processing parameters' optimization. (A-C) Crack propagation at the interface, (D) delamination, and macro-cracks of the built sample.

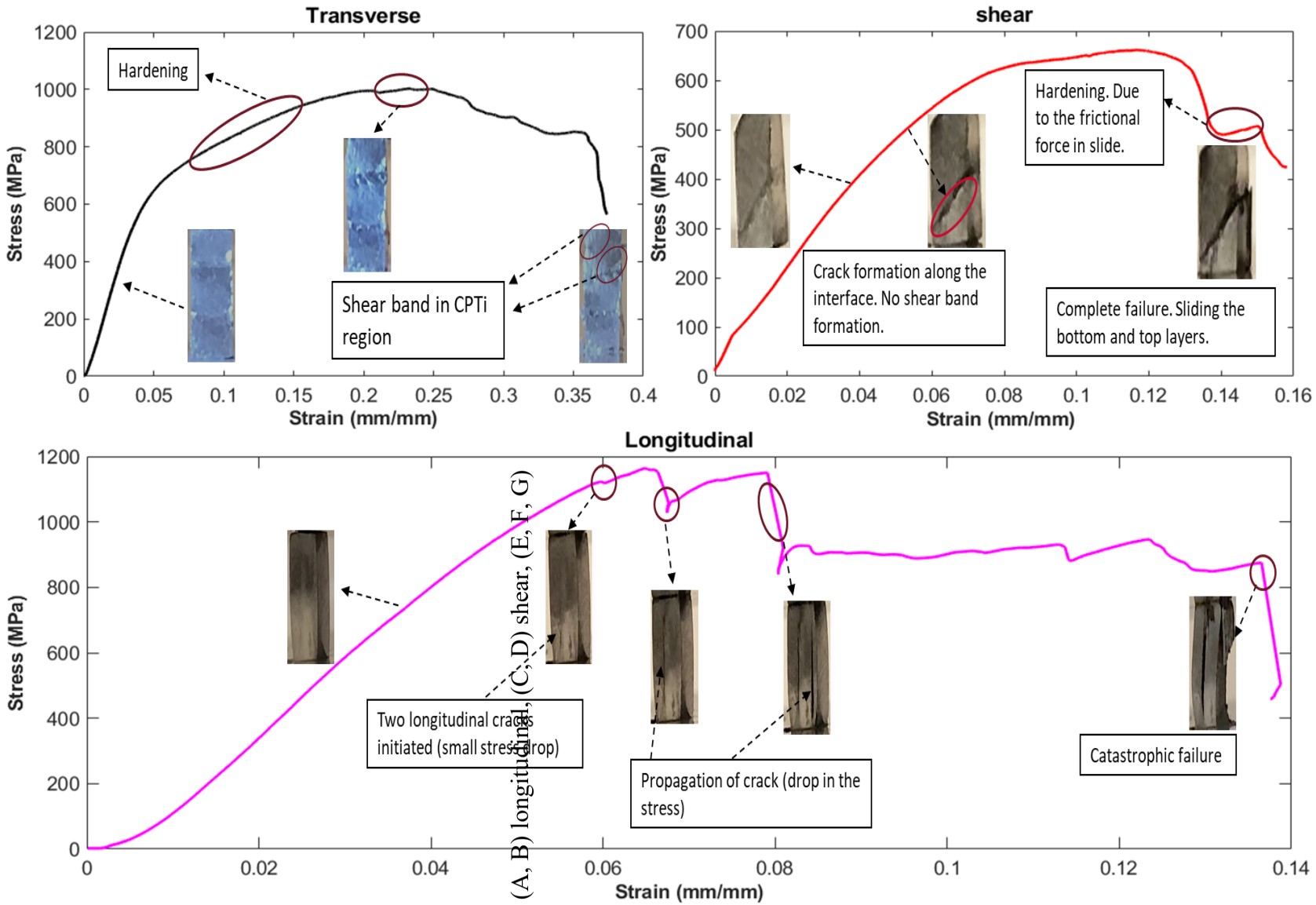

es from the damaged area. (A, B) longitudinal, (C, D) shear, (E, F, G)

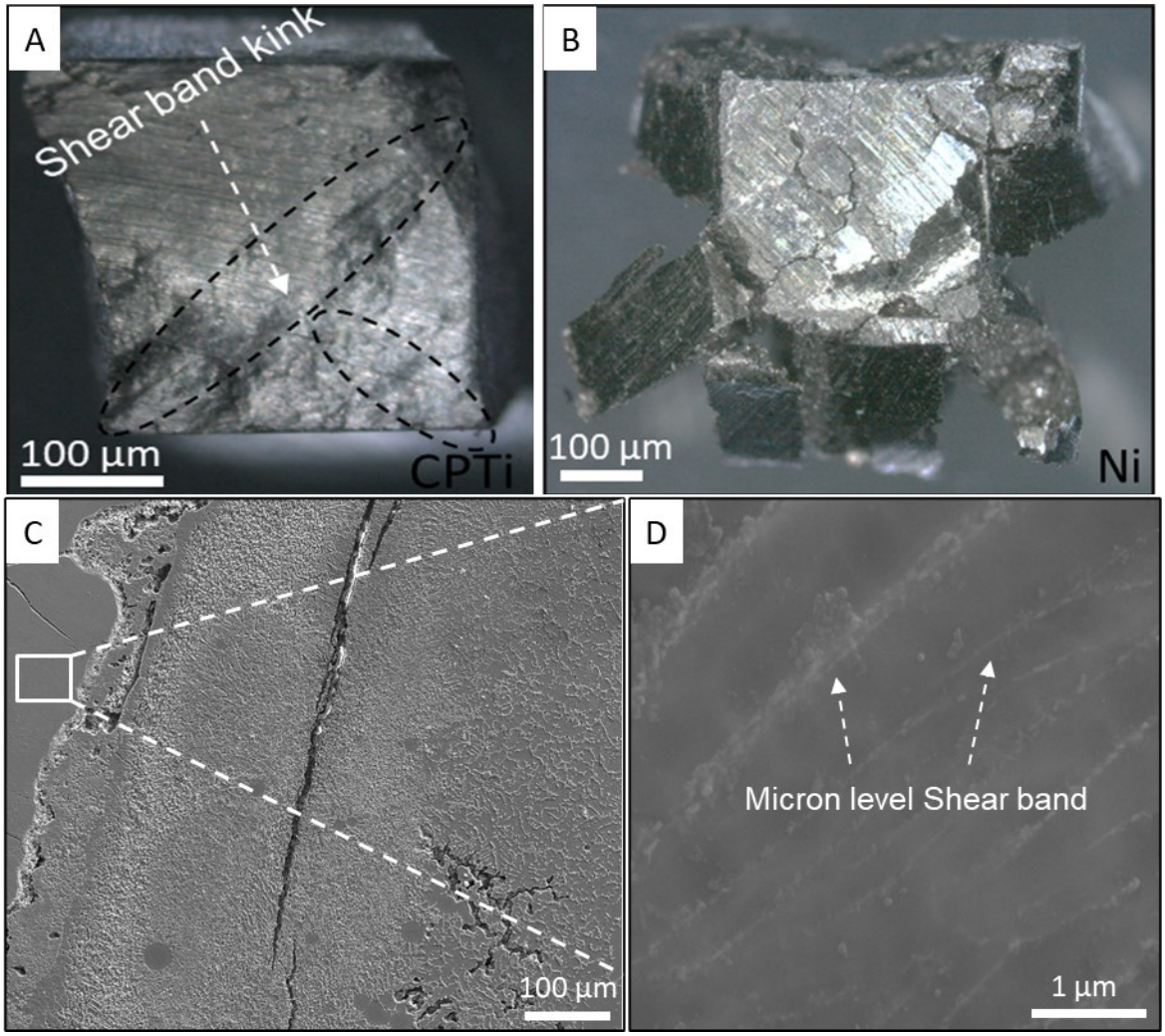

Fig. 11. (A, B) Failure of pure CP Ti and Nickel, (C, D) microscopic cracks and micron-level shear band formation in the after-test longitudinal sample.